The Astrophysical Journal Letters, 988:L23 (11pp), 2025 July 20 https://doi.org/10.3847/2041-8213/adea4f

Langmuir-wave Excitation in Solar Wind Magnetic Holes

Jingting Liu (刘婧婷)[1], Daniel Verscharen[1], Jesse Coburn[1,2], Georgios Nicolaou[1], Xiangyu Wu (吴翔宇)[1], Wence Jiang (蒋文策)[3], Oreste Pezzi[4], Francesco Pucci[4], Matteo Zuin[5,6], Christopher J. Owen[1], and Hamish Reid[1]
[1] Mullard Space Science Laboratory, University College London, Dorking RH5 6NT, UK
[2] The Blackett Laboratory, Imperial College London, London, SW7 2AZ, UK
[3] State Key Laboratory of Solar Activity and Space Weather, National Space Science Center, CAS, 100190, Beijing, People's Republic of China
[4] Istituto per la Scienza e Tecnologia dei Plasmi, Consiglio Nazionale delle Ricerche (ISTP-CNR), 70126 Bari, Italy
[5] Consorzio RFX (CNR, ENEA, INFN, Università di Padova, Acciaierie Venete SpA), 35127 Padova, Italy
[6] Istituto per la Scienza e la Tecnologia dei Plasmi del CNR, 35127 Padova, Italy
Received 2025 May 14; revised 2025 June 25; accepted 2025 June 27; published 2025 July 17

Abstract

Magnetic holes (MHs) are structures commonly observed in various space plasma environments throughout the solar system, including the solar wind. These structures are characterized by a localized decrease in magnetic field strength, coincident with an increase in plasma density. Previous observational studies in the solar wind link the presence of Langmuir waves to MHs, suggesting a strong correlation between these phenomena. We develop a model based on magnetic-moment conservation and its violation to explain the excitation of Langmuir waves in MHs. Our model illustrates that MHs induce changes in the electron velocity distribution function that emit electrostatic Langmuir waves due to the bump-on-tail instability. Using data from the Solar Orbiter spacecraft, we provide a comprehensive analysis of this process and test our predictions with observations. The consistency between our model and observations indicates that the proposed process is a viable mechanism for producing Langmuir waves in MHs in the solar wind.

Unified Astronomy Thesaurus concepts: Solar wind (1534); Space plasmas (1544)

1. Introduction

Magnetic holes (MHs) are localized regions in space plasmas in which the magnetic field strength decreases significantly, often by more than 50%. These structures were first identified in the solar wind (J. Turner et al. 1921). Since then, they have been observed across a variety of space environments, including planetary magnetosheaths (B. Tsurutani et al. 1982; E. Lucek et al. 1999), the Earth's cusp region (Q. Shi et al. 2009), planetary magnetotails (Y. Ge et al. 2011; W. J. Sun et al. 2012), and cometary environments (C. Russell et al. 1987). MHs vary in size, ranging from a few electron gyroradii ρ_e to thousands of proton gyroradii ρ_i (D. Winterhalter et al. 1994; K. Sperveslage et al. 2000). Several theories exist to explain the formation of MHs, including mirror-mode instabilities (B. Tsurutani et al. 1982; T. Zhang et al. 2008; T. Xiao et al. 2014), solitary waves (L. Burlaga & J. Lemaire 1978), interchange instabilities (G. Lapenta & L. Bettarini 2011), Kelvin–Helmholtz instability (G. Arrò et al. 2023), and turbulence (G. Arrò et al. 2024). MHs exhibit a higher density than the surrounding plasma in order to maintain pressure balance.

One of the ways in which MHs influence the plasma is through their interaction with waves: various types of waves are observed within MHs, including whistler waves (S. Yao et al. 2019; S. Huang et al. 2020; W. Jiang et al. 2022), electrostatic solitary waves (S. Yao et al. 2019), and electron cyclotron harmonic waves (X.-J. Zhang et al. 2017). These waves are absorbed or emitted through resonant interactions with different instability mechanisms linked to the trapped electron and ion populations inside the MHs (W. Jiang et al. 2024).

Langmuir waves (LWs) are electrostatic plasma waves with wave frequencies near and above the electron plasma frequency ω_{pe}. They are of particular interest for their fundamental role in converting energy through wave–particle interactions with electrons in weakly collisional plasmas such as the solar wind (W. Herr 2016). While interplanetary LWs are often associated with type II and type III radio bursts (I. H. Cairns 1986; P. Robinson & A. Benz 2000; M. Pulupa et al. 2020), a significant portion of LWs in the solar wind originate from MHs rather than radio bursts (N. Lin et al. 1996; J. Boldú et al. 2023). In fact, LWs occur more frequently in association with MHs than in the surrounding solar wind (J. Boldú et al. 2023).

The solar wind electron velocity distribution function (VDF) typically consists of a Maxwellian core, an isotropic suprathermal halo, and a field-aligned suprathermal strahl (W. Feldman et al. 1975; D. Verscharen et al. 2019b). The electron strahl is a skewed extension of the core population in the direction parallel or antiparallel to the magnetic field. It typically does not form a bump-on-tail configuration with a region of positive velocity gradient of the electron distribution. Hence, the strahl population is unlikely to generate electrostatic bump-on-tail instabilities in the ambient solar wind (K. Horaites et al. 2018; D. Verscharen et al. 2019a; J. M. Schroeder et al. 2021).

We propose that MHs can modify the strahl electron configuration in such a way that a local bump-on-tail distribution develops within the MH. This bump-on-tail configuration then drives LWs through resonant wave–particle interactions. Our model is based on the conservation of adiabatic invariants.

2. A Model for LW Generation in MHs

We first briefly introduce the bump-on-tail instability of LWs and the conservation of the magnetic moment μ conceptually. We then discuss the breaking of μ conservation and present our model for the modification of the electron VDF due to the breaking of μ conservation in MHs.

2.1. Bump-on-tail Instability

The bump-on-tail instability arises when the local gyrotropic particle VDF $f(v_\perp, v_\parallel)$ develops a beam signature in such a way that $\partial f/\partial v_\parallel > 0$ at $v_\parallel > 0$ or $\partial f/\partial v_\parallel < 0$ at $v_\parallel < 0$, where $v_\perp$ and $v_\parallel$ denote the perpendicular and parallel velocity components with respect to the local magnetic field direction. For the sake of simplicity but without loss of generality, we limit our analysis to the case in which $\partial f/\partial v_\parallel > 0$ at $v_\parallel > 0$.

Plasma waves with a phase speed $v_{\rm phase} = \omega/k_\parallel$ can Landau-resonate with particles at $v_\parallel = v_{\rm phase}$, where ω is the real part of the wave frequency and $k_\parallel$ is the component of the wavevector parallel to the background magnetic field. If this Landau resonance occurs in the region of velocity space where $\partial f/\partial v_\parallel > 0$, the resonant interaction converts particle energy into wave energy, leading to wave growth (W. Baumjohann & R. A. Treumann 1996). The inverse process, in which the waves lose energy to the particles, corresponds to Landau damping.

We approximate the LW dispersion relation through the Bohm–Gross approximation (F. F. Chen 2016),

$$\omega^2 \approx \omega_{\rm pe}^2 + \frac{3}{2} k_\parallel^2 v_{\rm th,e}^2, \tag{1}$$

where $v_{\rm th,e} = \sqrt{2k_{\rm B}T_{\rm e}/m_{\rm e}}$ is the electron thermal speed, $k_{\rm B}$ is the Boltzmann constant, $T_{\rm e}$ is the electron temperature, and $m_{\rm e}$ is the electron mass.

In the majority of solar wind intervals, strahl electrons are located very close to the core, thus not forming a positive velocity gradient in the VDF. Electron distributions, in the absence of energetic electron beams, are therefore unlikely to show a bump-on-tail configuration.

Equation (1) indicates that the second term $\propto v_{\rm th,e}^2$ plays an increasingly significant role as $k_\parallel$ increases. For $k_\parallel \to \infty$, the dispersion relation asymptotically approaches $v_{\rm phase} = \sqrt{3/2}\, v_{\rm th,e}$. Consequently, the bump-on-tail instability can only occur if $\partial f/\partial v_\parallel > 0$ at $v_\parallel > v_{\rm phase} = \sqrt{3/2}\, v_{\rm th,e}$ (see also K. Pommois et al. 2017).

2.2. The First Adiabatic Invariant: Magnetic Moment μ

When electrons traverse regions with inhomogeneous magnetic fields, their velocity distribution adjusts in response to these variations. The electrons conserve their magnetic moment μ, which is the first adiabatic invariant, during this evolution when the electrons are magnetized and changes in the magnetic field are slow compared to the electron gyration. The magnetic moment μ is associated with the current created by the gyration of the electron (S. Ichimaru 1973) and is given by

$$\mu = \frac{m_{\rm e} v_\perp^2}{2B}, \tag{2}$$

where B is the magnetic field strength.

When the magnetic field strength increases, conservation of μ demands that $v_\perp^2$ increases as well. The kinetic energy

$$E = \frac{1}{2} m_{\rm e} (v_\perp^2 + v_\parallel^2) \tag{3}$$

remains conserved as long as no electric field is present. Therefore, $v_\parallel^2$ must decrease as $v_\perp^2$ increases. This effect leads to magnetic mirroring in a spatially increasing B field when particles cross $v_\parallel = 0$. Localized depletions in B, such as MHs, are by definition bordered by regions with increasing B on both sides, suggesting that mirroring occurs on both sides. Particles that mirror on both sides of an MH are trapped in this structure.

Particles with small $|v_\perp/v_\parallel|$ are not mirrored but instead move along the field lines. They enter and leave localized depletions in B. The loss cone defines the region in velocity space that is occupied by particles that leave localized depletions in B. Particles outside the loss cone form the trapped population. We define the loss-cone angle α through (F. F. Chen 2016)

$$\sin^2 \alpha = \frac{B}{B_{\rm max}}, \tag{4}$$

where $B_{\rm max}$ is the maximum magnetic field strength of the structure. A particle is not mirrored if its pitch angle ϕ satisfies $\sin^2\phi < \sin^2\alpha$, where $\tan\phi = v_\perp/v_\parallel$.

2.3. Breaking of μ Conservation

Formally, an electron must fulfill two conditions in order to conserve its magnetic moment when passing an inhomogeneous magnetic field structure: (i) the particle gyroradius must be smaller than the size of the magnetic structure, and (ii) the particle must be able to complete at least one gyration while crossing the structure in order to remain magnetized.

Both conditions are fundamentally tied to the magnetic field geometry. To formulate these conditions mathematically, we first estimate the spatial size $R_{\rm c}$ of the field variation associated with the structure as

$$\frac{1}{R_{\rm c}} \sim \left| \frac{1}{B} \frac{{\rm d}B}{{\rm d}s} \right|, \tag{5}$$

where s is the spatial coordinate along the structure. We assume that the structure is in a steady state and propagates with the same speed as the proton bulk flow across our measurement point. According to Taylor's hypothesis and the frozen-in theorem (W. Baumjohann & R. A. Treumann 1996), we relate spatial derivatives to time derivatives in spacecraft measurements using the proton speed $U_{\rm p}$ as

$$\frac{d}{ds} = \frac{1}{U_{\rm p}} \frac{d}{dt}. \tag{6}$$

Therefore,

$$\frac{1}{R_{\rm c}} \sim \left| \frac{1}{B} \frac{dB}{ds} \right| \approx \left| \frac{1}{BU_{\rm p}} \frac{dB}{dt} \right| = \left| \frac{1}{U_{\rm p}} \frac{\rm d}{dt} \ln B \right|. \tag{7}$$

With this estimate for the size of the structure, we express condition (i) as

$$r_{\rm g} \lesssim R_{\rm c}, \tag{8}$$

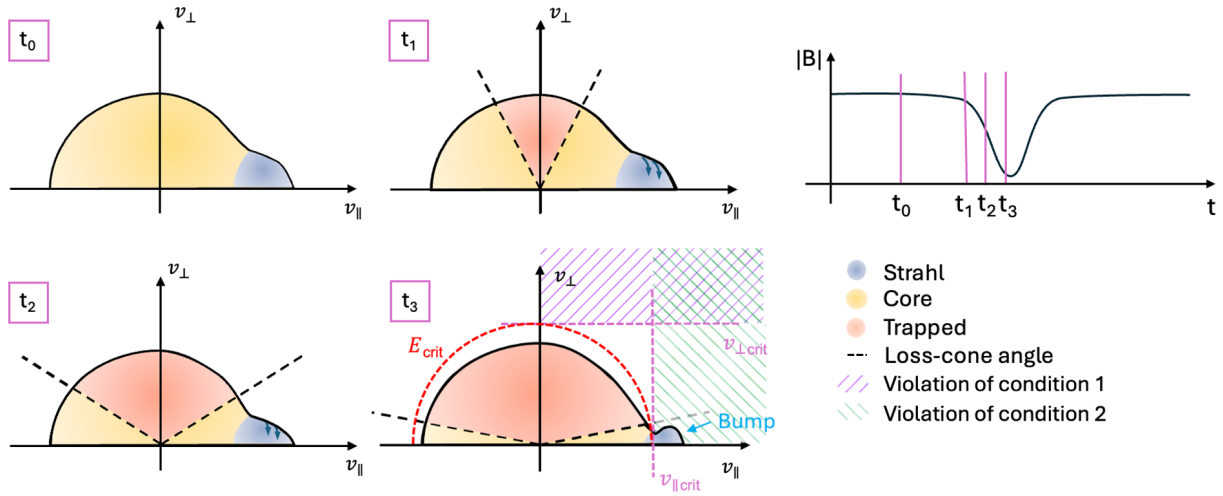

Figure 1. Illustration of changes in the electron VDF when passing through an MH. The variation in magnetic field strength as a function of time is shown on the right, with the times of interest indicated by pink lines. Time t_0 corresponds to the time before entering the MH. Electrons with $v_\parallel > 0$ stream toward the MH with a core and strahl configuration, while the distribution at $v_\parallel < 0$ consists of core electrons that have already crossed the MH. For the subsequent times, the loss-cone angle α is represented by black dashed lines. The distribution functions at t_1, t_2, and t_3 illustrate the VDFs at their respective locations within the MH. Near the minimum of $|B|$ at t_3, strahl electrons with velocities within the shaded area violate their μ conservation. These electrons have energy greater than the critical energy $E_{\rm crit}$ and form a bump in the form of a positive gradient in velocity space.

where $r_{\rm g} = m_{\rm e} v_\perp c/eB$ is the electron gyroradius, c is the speed of light, and e is the elementary charge. We rewrite condition (i) under the assumption that $U_{\rm p} > 0$ as

$$\sin\phi \lesssim \frac{U_{\rm p}}{\left|\frac{d\ln B}{dt}\right|}\frac{eB}{c}\sqrt{\frac{1}{2m_{\rm e}E}}. \tag{9}$$

We write condition (ii) as

$$\tau \gtrsim \frac{1}{\Omega_e}, \tag{10}$$

where τ is the crossing time of a given electron through the structure and $\Omega_e = eB/m_{\rm e}c$ is the electron cyclotron frequency. We estimate the time taken by a particle to cross the structure as

$$\tau \sim \frac{R_{\rm c}}{v_\parallel} \sim \frac{U_{\rm p}}{\left|\frac{d\ln B}{dt}\right|}\sqrt{\frac{m_{\rm e}}{2E}}\frac{1}{\cos\phi}. \tag{11}$$

Therefore, we find that condition (ii) is fulfilled if

$$\cos\phi \lesssim \frac{U_{\rm p}}{\left|\frac{d\ln B}{dt}\right|}\frac{eB}{c}\sqrt{\frac{1}{2m_{\rm e}E}}. \tag{12}$$

Both conditions, as expressed in Equations (9) and (12), define pitch-angle ranges at given energies E in which the conditions are fulfilled, depending on the properties of the magnetic field structure. The left-hand sides of both equations are bounded between 0 and 1 when $v_\parallel > 0$. The right-hand sides of Equations (9) and (12) are greater than 1 in most cases in the solar wind, indicating that μ is conserved most of the time.

When particles encounter an MH, one or both of these conditions can be violated. In a deep MH, the magnetic field strength B decreases significantly. In addition, if the change of the magnetic field occurs on a small spatial scale, $|{\rm d}\ln B/{\rm d}t|$ is large, corresponding to a sharp MH. These two scenarios, deep MHs and sharp magnetic field gradients, may occur individually or simultaneously, potentially lowering the right-hand sides of Equations (9) and (12) to values between 0 and 1. When this occurs, the conservation of the magnetic moment in the structure is violated.

For constant B and ϕ, electrons at higher E are more likely to break μ conservation according to these conditions. We define the maximum energy required to fulfill Equations (9) and (12) as

$$E_{\rm crit} = \frac{m_{\rm e}}{2}\left(\frac{U_p}{\frac{d\ln B}{dt}}\right)^2\left(\frac{eB}{m_{\rm e}c}\right)^2. \tag{13}$$

All electrons with $E \geqslant E_{\rm crit}$ have the potential to break μ conservation at a specific pitch angle.

When one or both conditions are not satisfied for electrons in a given part of velocity space, these electrons are no longer magnetized, and these electrons do not follow the adiabatic μ conservation anymore. We assume that these particles tend to remain in their original position in velocity space rather than being modified by the constraints imposed by the conservation of μ.

2.4. Modification of VDF Due to Breaking of μ Conservation

We now examine the effects of the breaking of the μ conservation on the overall electron VDF, with a particular focus on the strahl population. We illustrate our model in Figure 1.

We build a scenario in which a spacecraft travels through a symmetric MH, as illustrated in the right panel of Figure 1. At time t_0, we measure an electron distribution function for which electrons with $v_\parallel > 0$ move toward the MH and electrons with $v_\parallel < 0$ have already traversed the structure. The strahl electrons in blue move toward the MH.

As electrons travel through the MH, they first encounter a reduction in the magnetic field strength. To conserve their magnetic moment μ, the particles' perpendicular velocity decreases. In response, their parallel velocity increases to

maintain the conservation of E. This change in magnetic field strength alters the VDF, causing the pitch angle of the electrons to decrease. This effect has no impact on the isotropic core electron population, as their f depends on v^2 only. In contrast, strahl electrons are significantly influenced by the μ conservation. At time t_1, the strahl electrons occur at smaller pitch angles compared to their occurrence at t_0.

Electrons outside the loss cone are trapped within the MH. As our spacecraft moves to regions of decreasing magnetic field strength, the loss-cone angle decreases and the area of velocity space occupied by trapped electrons expands. Electrons originating from outside the MH are always within the loss cone, assuming they behave adiabatically, which allows them to enter and leave the structure. As they pass through the MH, these electrons experience a reduction in their pitch angles until they reach the bottom of the MH; however, they return to their initial velocity space coordinates when leaving the MH on the other side.

At time t_3, we encounter the VDF at the minimum of B. At this point, the μ conservation is violated for the part of the electron VDF that does not satisfy Equations (8) and (10). By rearranging Equations (9) and (12), we express the conditions in terms of critical velocities:

$$v_{\perp,\mathrm{crit}} = \sqrt{\frac{2E_{\mathrm{crit}}}{m_e}}\sin(90^\circ) = \sqrt{\frac{2E_{\mathrm{crit}}}{m_e}} \tag{14}$$

and

$$v_{\parallel,\mathrm{crit}} = \sqrt{\frac{2E_{\mathrm{crit}}}{m_e}}\cos(0^\circ) = \sqrt{\frac{2E_{\mathrm{crit}}}{m_e}}. \tag{15}$$

We indicate the velocity space at $v_\parallel \geqslant v_{\parallel,\mathrm{crit}}$ and $v_\perp \geqslant v_{\perp,\mathrm{crit}}$ as shaded areas in Figure 1 for time t_3, suggesting that any particles with velocities exceeding these critical values can violate the μ conservation. The adiabatic evolution of f is restricted to the region where the conservation of μ is maintained. As per our assumption, strahl electrons that do not conserve μ anymore tend to appear at larger pitch angles than expected from μ conservation. If this deviation occurs near or above the transition from the core to the strahl part of the VDF, it can create a positive velocity gradient in the distribution function. When $\partial f/\partial v_\parallel > 0$ at velocities exceeding the bump-on-tail instability threshold v_{thr}, the bump on the VDF can drive the Landau-resonant instability of LWs.

3. Observations

With the advent of the new space missions Solar Orbiter and Parker Solar Probe, MHs are now being studied in environments close to the Sun, where background magnetic field strengths and plasma conditions differ significantly from near-Earth space (C. Chen et al. 2021; L. Yu et al. 2021; J. Boldú et al. 2023). The data from these missions allow us to study the kinetic properties of MHs in great detail.

3.1. Overview

The data set used for our research is collected from three instruments on board Solar Orbiter: the Solar Wind Analyser (SWA), the Radio and Plasma Waves (RPW) instrument, and the Magnetometer (MAG). The Electron Analyser System (EAS) is part of the SWA suite and measures solar wind electrons at energies from a few eV to 5000 eV, providing detailed three-dimensional VDFs; the Proton-Alpha Sensor (PAS) is also part of SWA and measures the VDFs of protons and α-particles (C. Owen et al. 2020, 2021). The RPW instrument captures variations in the electric and magnetic fields. It is capable of measuring in situ waves with frequencies up to several hundred kHz. RPW's Thermal Noise Receiver (TNR) delivers electromagnetic spectra from several kHz to 16 MHz, and its Time Domain Sampler (TDS) serves as a medium-frequency receiver dedicated to capturing waveform data (M. Maksimovic et al. 2020; J. Soucek et al. 2021). The MAG instrument records vector magnetic field data at a sampling rate of 128 vectors s^{-1} (T. Horbury et al. 2020). These instruments collectively provide the high-resolution measurements adopted for this investigation.

Based on our model presented in Section 2.2, we identify two MH events in which the minimum magnetic field strength, as measured by the MAG instrument, decreases below 1 nT.

3.2. Case 1

As illustrated in Figure 2, the magnetic field strength drops from 5.723 nT at 00:24:05 UT to 0.253 nT at 00:24:49 UT. The black lines in the pitch-angle spectrum shown in panel (c) represent the loss-cone angles calculated with Equation (4). We observe that the VDF values outside the loss cone (i.e., within the black lines) are greater than inside, indicating the presence of an enhanced trapped electron population. Panel (f) shows a magnetic field feather plot to provide additional context for the local magnetic field structure.

We calculate Equations (9) and (12) throughout the time interval for this event, covering an energy range from 69 eV to 2000 eV. To estimate the size of the MH structure, we apply Equation (7), using magnetic field measurements and proton speed measurements obtained from MAG and SWA/PAS. Within this energy range, electrons can only break our conditions for μ conservation during the period of minimum magnetic field strength (occurring at 00:24:49 UT) with $E_{\mathrm{crit}} \approx 1130$ eV. The corresponding pitch-angle solutions from Equations (9) and (12) are overplotted in panels (c) and (d) as blue and olive data points.

In panel (d), we present the pitch-angle distribution for electrons in the energy range around E_{crit}, spanning from 1000 eV to 1500 eV. We select this energy range around the calculated value of E_{crit} to account for uncertainties in our model predictions and to include more electron counts at high energies. We discuss the impact of finite particle counting statistics on our observational results in Section 4.2. This panel reveals a group of electrons with phase-space density significantly greater than the surrounding average, particularly at times near the minimum B. At the same time, when Equations (9) and (12) are not satisfied, RPW detects an enhancement in the electric field fluctuations at approximately 20 kHz, as shown in panel (e).

We show three instances of the two-dimensional electron VDF as a function of speed v and pitch angle ϕ in Figure 3. The first panel shows the VDF before the strahl electrons enter the MH. The second panel shows the VDF at the location of the minimum in the magnetic field strength. The third panel shows the VDF after the strahl electrons have left the MH. These measurements reveal the evolution of the electron VDF. Before the strahl enters the MH (left) and after the strahl exits the MH (right), the VDFs exhibit similar distributions, both showing enhanced electron fluxes at small pitch angles around $\phi \gtrsim 0^\circ$. At the location of the recorded minimum magnetic

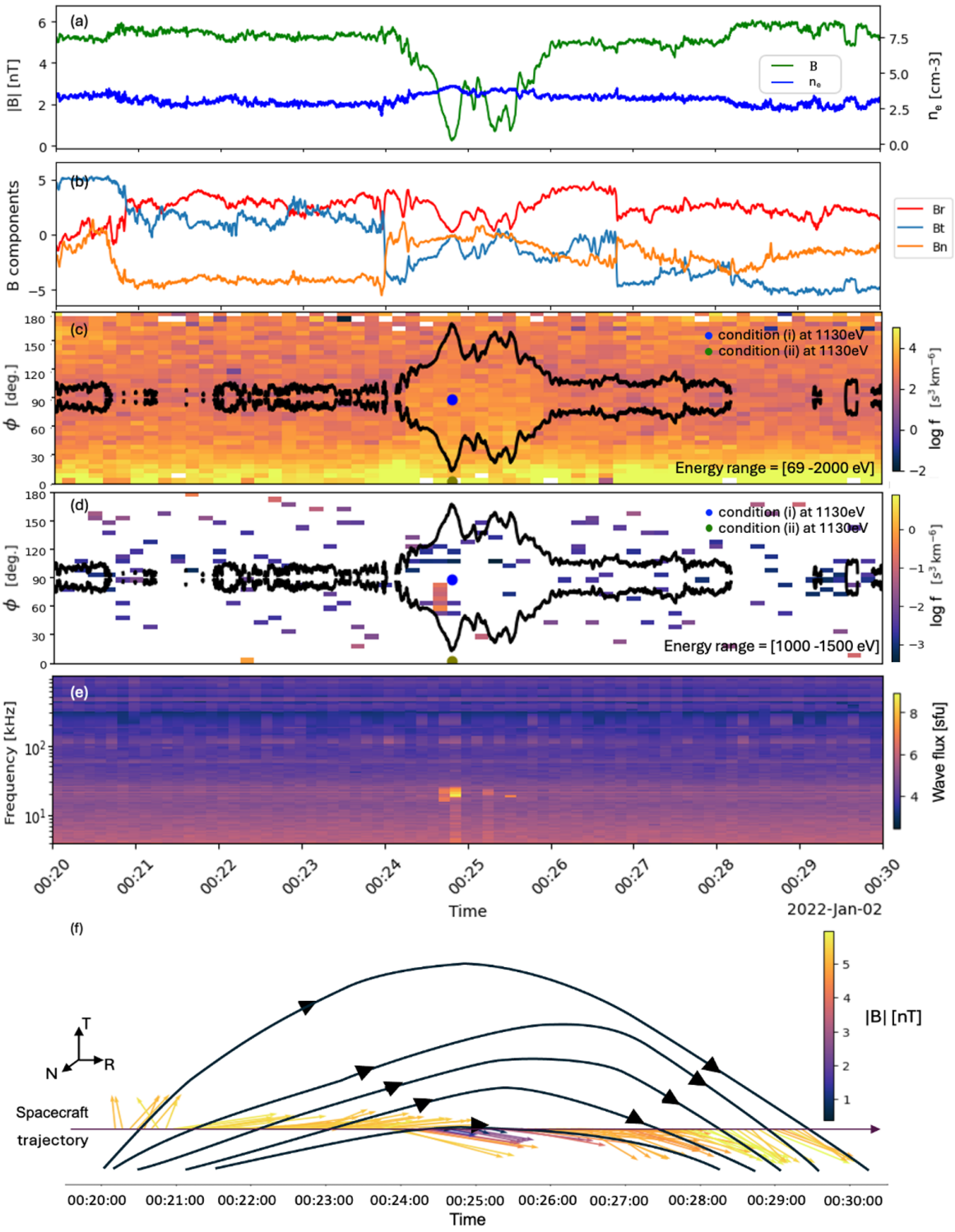

Figure 2. Solar Orbiter observations of an MH on 2022 January 2 from 00:20:00 UT to 00:30:00 UT (case 1). The horizontal axis shows the time in UT (hh:mm). (a) Magnetic field strength B in green and electron number density n_e in blue. (b) Components of the magnetic field in RTN coordinates, where R is the radial direction, T is the tangential direction, and N completes the right-handed triad. (c) Electron pitch-angle distribution of electrons from 69 eV to 2000 eV. (d) Electron pitch-angle distribution from 1000 eV to 1500 eV. The blue and olive colored dots indicate angles beyond which Equations (9) and (12) are violated for $E = E_{\rm crit} = 1130$ eV. (e) Dynamic spectrum of wave flux vs. time in spectral flux units. (f) Illustration of a possible magnetic field configuration based on a feather plot of our in situ magnetic field measurements. In this panel, time is displayed in hh:mm:ss format.

field strength (center), we observe fewer electrons around $\phi \gtrsim 0^\circ$ and more electrons at higher energies and ϕ. At the same time, the loss-cone angle reaches the range of pitch angles occupied by strahl electrons.

Based on our model, we assume that the resonance velocity of LWs is near $v_{\parallel,\rm crit}$. By substituting $v_{\parallel,\rm crit}$ into Equation (1), we predict an LW frequency of approximately 19 kHz at resonance. The resonance condition is fulfilled for those waves

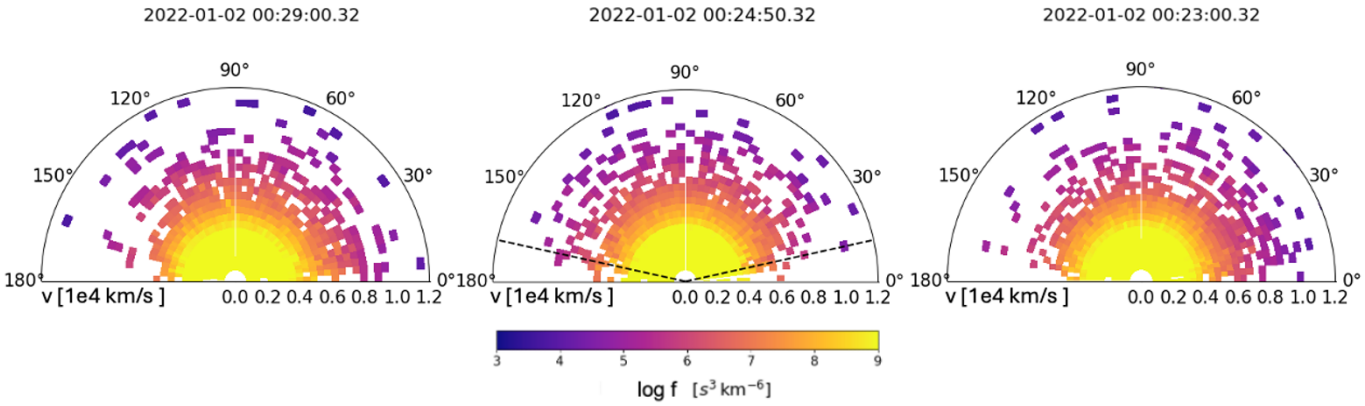

Figure 3. Electron VDFs at three characteristic phases for case 1: (left) before the strahl population enters the MH, (center) at the time of the recorded minimum magnetic field strength with the loss-cone angle indicated by black dashed lines, and (right) after the strahl population exits the MH. The corresponding times in UT (hh:mm:ss) are indicated above each panel. The angles indicate the pitch angle ϕ.

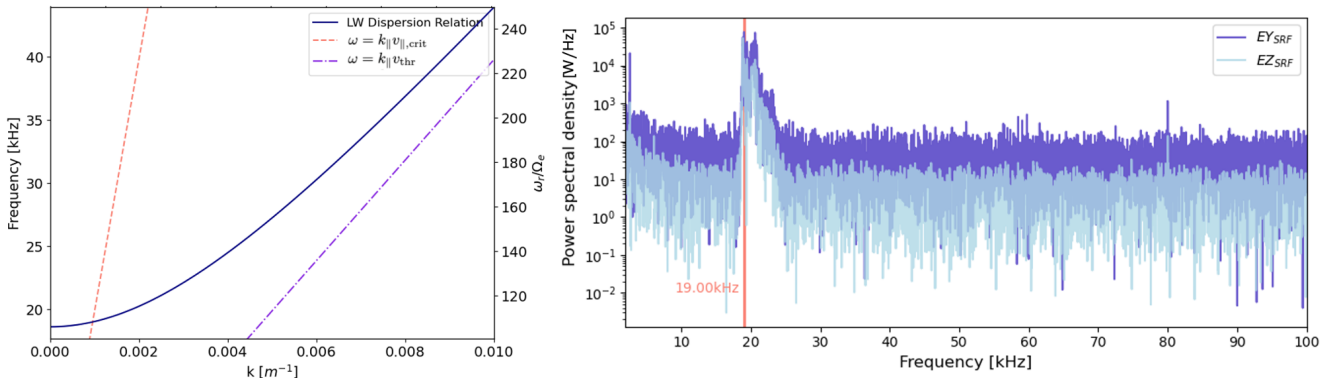

Figure 4. Left: LW dispersion relation from Equation (1) for case 1. We overplot the resonance condition $\omega = k_\parallel v_{\parallel,\mathrm{crit}}$ for $E_{\mathrm{crit}} = 1130$ eV in orange. The purple line shows $\omega = k_\parallel v_{\mathrm{thr}}$. Right: triggered snapshot waveform from the RPW-TDS instrument, data captured at 00:24:52.79 UT on 2022 January 2 (case 1). EY_{SRF} and EZ_{SRF} represent the electric field components measured along the *Y*- and *Z*-axes in the spacecraft reference frame.

in Figure 4 (left) for which the plot of the dispersion relation intersects the line marking $\omega = k_\parallel v_{\parallel,\mathrm{crit}}$.

The RPW-TDS captures the waveform of the observed waves, as shown in the right panel of Figure 4, offering higher-resolution electric field measurements. This panel displays the power spectrum of the captured waveform, revealing the actual observed wave frequency. We mark the predicted resonant frequency in the panel on the right-hand side of Figure 4 with an orange vertical line. The spectrum shows a clear enhancement of electric field fluctuations at and above the predicted resonant frequency.

3.3. Case 2

We study a second case of an MH associated with electric field fluctuations that are consistent with our model predictions. Figures 5, 6, and 7 present the same contents for case 2 as Figures 2, 3, and 4 present for case 1. This MH has a shorter duration in the spacecraft frame. The magnetic field decreases from 4.75 nT at 08:01:43 UT. The field strength reaches its minimum value of 0.177 nT at 08:01:49 UT. As shown in panel (f) of Figure 5, the consistently interpreted magnetic structure based on the feather plot of the magnetic field differs notably from that of case 1.

The decrease in B occurs more rapidly compared to case 1, resulting in a smaller $E_{\mathrm{crit}} \approx 150$ eV. In panel (d), we plot the electron pitch-angle distribution over the energy range of 100–250 eV. We observe that the electron VDF values at larger pitch angles are slightly greater inside the MH than before and after the MH event.

The dynamic spectrum in panel (e) does not show a clear enhancement during this time interval. However, the TDS triggered waveform snapshot successfully observes activity at frequencies around 15.7 kHz as shown in Figure 7.

The two-dimensional VDFs in Figure 6 show a similar trend to case 1: enhanced higher-energy particle fluxes at larger pitch angles around the time of the recorded minimum in B (center panel). At the same time, the loss-cone angle reaches the pitch-angle range occupied by strahl electrons. This observation is consistent with the electron dynamics shown in panel (d) of Figure 5.

For $E_{\mathrm{crit}} \approx 150$ eV, the LW dispersion relation from Equation (1) predicts a resonant frequency of approximately 15.7 kHz. This predicted frequency is indicated by the orange vertical line in the right panel of Figure 7, superimposed on the observed waveform snapshot. The captured waveform exhibits a peak at 15.25 kHz, which approximately aligns with our prediction based on the resonance condition and the dispersion relation for LWs.

4. Discussion

In this section, we provide our interpretation and further implications of our study. We discuss the limitations of our analysis and provide alternative scenarios.

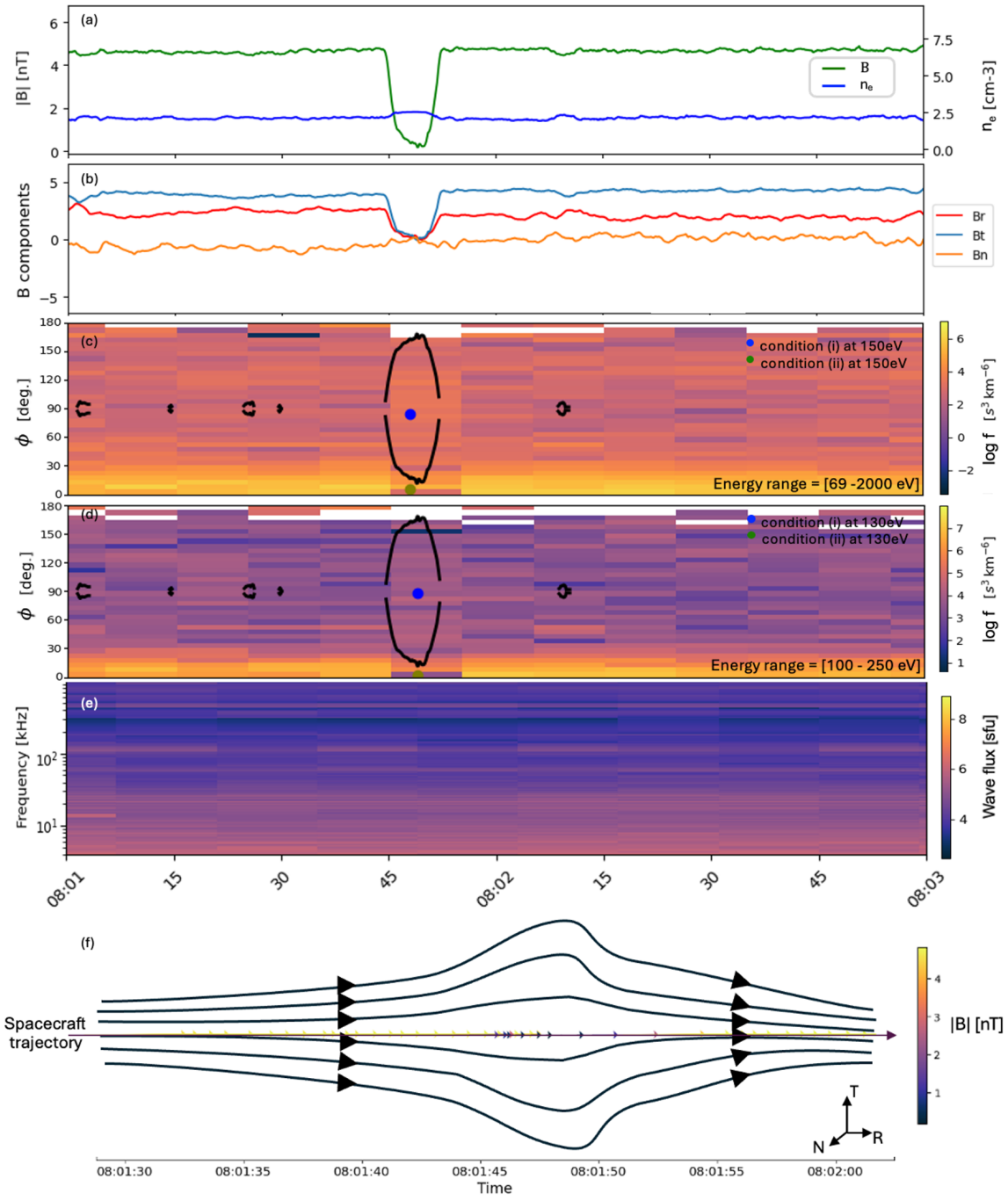

Figure 5. Solar Orbiter observations of an MH on 2022 January 2 from 00:08:01 UT to 00:08:03 UT (case 2). The horizontal axis shows the time in UT (hh:mm). (a) Magnetic field strength B in green and electron number density n_e in blue. (b) Components of the magnetic field in RTN coordinates. (c) Electron pitch-angle distribution of electrons from 69 eV to 2000 eV. (d) Electron pitch-angle distribution from 100 eV to 250 eV. The blue and olive colored dots indicate angles beyond which Equations (9) and (12) are violated for $E = E_{\rm crit} = 150$ eV. (e) Dynamic spectrum of wave flux vs. time in spectral flux units. (f) Illustration of a possible magnetic field configuration based on a feather plot of our in situ magnetic field measurements. In this panel, time is displayed in hh:mm:ss format.

4.1. Interpretation and Implications of Our Results

Previous studies report LWs associated with magnetic depressions, with most cases occurring in MHs (N. Lin et al. 1995, 1996; R. MacDowall et al. 1996; J. Boldú et al. 2023). We present a model for the creation of LWs in MHs based on the violation of μ conservation for strahl electrons in the solar wind. Our model establishes threshold criteria in both pitch angle and energy for the violation of μ conservation. We present observations from Solar Orbiter that are consistent with the earlier observations of LWs near MHs and align with the predictions of our model.

In the two cases we present, we find enhancements in electrostatic fluctuations during short periods of low magnetic field strength. These enhancements occur at times at which our model predicts the violation of μ conservation for strahl electrons. The observations are consistent with our proposed process of the creation of a bump-on-tail configuration that triggers LWs.

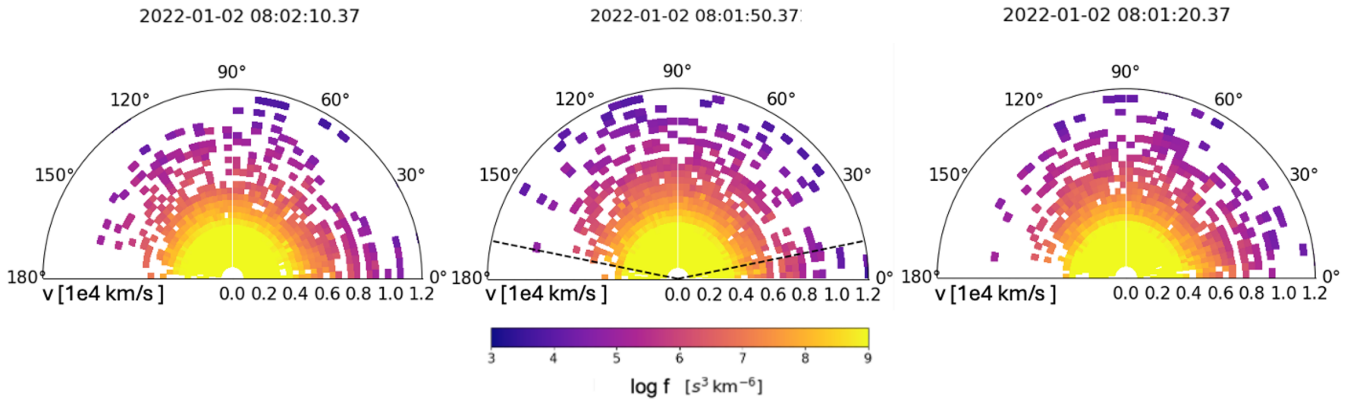

Figure 6. Electron VDFs at three characteristic phases for case 2: (left) before the strahl population enters the MH, (center) at the time of the recorded minimum magnetic field strength with the loss-cone angle indicated by black dashed lines, and (right) after the strahl population exits the MH. The corresponding times in UT (hh:mm:ss) are indicated above each panel. The angles indicate the pitch angle ϕ.

In case 1, the MH has a longer duration in the spacecraft reference frame, allowing us to resolve more details of the particle dynamics. We observe multiple LW events within the overall interval of case 1. Most notably, a significant enhancement in LW activity coincides with the minimum of the recorded magnetic field strength, in agreement with our model prediction. Under quiet conditions, LWs usually arise as quasi-thermal noise caused by thermal electron motion, producing weak electrostatic fluctuations. The quasi-thermal noise forms peaks in the power spectrum near the plasma frequency (G. Le Chat et al. 2009). The observed LW event at the time of the minimum of B, however, produces a clear enhancement of electrostatic fluctuations above the level of the quasi-thermal noise. While our model cannot predict all LW occurrences (as the physical mechanism may operate in regions beyond the spacecraft's trajectory), the clear enhancement of LWs at the field minimum offers a strong validation of our theoretical framework.

In case 2, no clear LW signal is detected in the RPW-TDS radio spectrum, but the RPW-TNR captures a signature of LWs coinciding with the MH. This discrepancy may be due to the low time resolution of RPW-TNR. The TDS-tswf mode is designed to capture high-time-resolution data and is sensitive to transient phenomena. The MH in case 2 is shorter in duration in the spacecraft frame and exhibits a sharper magnetic gradient compared to case 1. The resulting increase in R_c leads to solutions to Equations (8) and (10) at lower energy levels. The wider energy range in case 2 allows more electrons to break μ conservation, potentially causing them to occupy a larger range of pitch angles. However, this does not necessarily help the development of a bump-on-tail configuration, as the increased population of electrons at lower energy levels may just raise the VDF values without creating a distinct positive gradient in f. Alternatively, a small bump may form, but it may not generate sufficiently large LW amplitudes, above the thermal noise, to be clearly detected by RPW-TNR.

Only particles above a specific energy can satisfy the condition for the breaking of μ conservation in an MH. Most MHs have a minimum B of about 0.1 nT, so that electrons with energies exceeding 10^2 eV are more likely to meet the criteria. This energy threshold is significantly greater than the threshold energy required for the bump-on-tail instability, represented by v_{thr}. Therefore, it is likely that strahl electrons in MHs above E_{crit}, as long as they are present in sufficient number, effectively trigger LWs through our proposed mechanism. We note, however, that a locally anisotropic velocity distribution above E_{crit} is required for our model to explain the driving of LWs, as an isotropic distribution would not produce the necessary positive gradient in velocity space for the excitation of the bump-on-tail instability.

According to our conditions for the violation of μ conservation, deep or sharp MHs are more likely to trigger LWs. However, not all deep or sharp MHs are observed in association with LWs. We attribute this observation to the number of electrons that meet the criteria to break μ conservation. When there are too few resonant particles in the relevant part of velocity space, their energy transfer to LWs will result in fluctuations below the detection threshold. The calculated E_{crit} varies widely depending on the specific MH. A large E_{crit} is not always favorable for our mechanism, as the number of particles participating in the violation of the magnetic moment is small. However, if a bump-on-tail instability is triggered, the resonant velocity is likely to occur at energies close to E_{crit}, as observed in case 1 of our study. In contrast, a small E_{crit} value allows more electrons to violate μ conservation.

Particles that break μ conservation can cross the trapping angle from the loss cone into the trapped region of velocity space. Moreover, if LWs are excited, quasilinear diffusion reduces the $v_{\parallel}$ of the resonant electrons (D. Verscharen et al. 2022), causing their phase-space distribution to migrate toward the thermal core population. When these processes move particles from the loss cone into the trapped region of velocity space, they serve as an additional source of the trapped population, feeding more particles into the structure.

4.2. Limitations of Our Analysis

MHs are not static structures (G. Helgesen et al. 1990; W. Jiang et al. 2022). Estimating their size and predicting their evolution based on single-spacecraft measurements is very challenging. As a result, our calculation of E_{crit} based on the steady-state assumption and our estimate of R_c provide only an approximate result. In fact, the properties of the magnetic field significantly influence our calculations. We estimate the size of the field depletion associated with the MH using the proton speed U_p, and the change in the magnetic field strength is

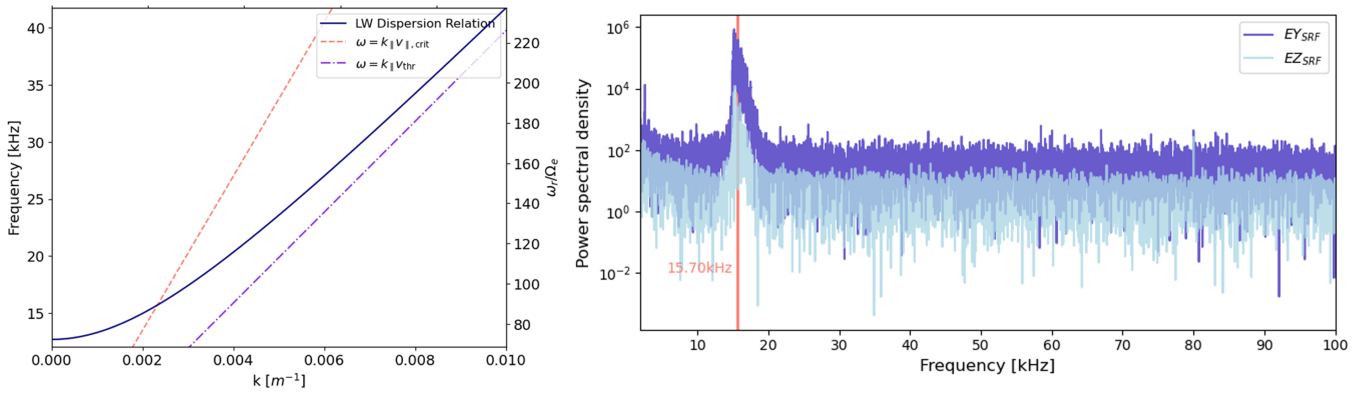

Figure 7. Left: LW dispersion relation from Equation (1) for case 2. We overplot the resonance condition $\omega = k_\parallel v_{\parallel,\mathrm{crit}}$ for $E_{\mathrm{crit}} = 150$ eV in orange. The purple line shows $\omega = k_\parallel v_{\mathrm{thr}}$. Right: triggered snapshot waveform from the RPW-TDS instrument, data captured at 08:01:45.84 UT on 2022 January 2 (case 2). EY_{SRF} and EZ_{SRF} represent the electric field components measured along the Y- and Z-axes in the spacecraft reference frame.

measured in the spacecraft reference frame. Both factors affect the determination of R_c. A precise calculation of R_c would require detailed knowledge of the three-dimensional MH geometry, which is unavailable from single-spacecraft measurements. In this vein, we interpret our formulation of condition (i) and condition (ii) as approximate indicators for the potential breaking of μ conservation rather than a rigid prediction of this process.

Higher-resolution data would significantly enhance our understanding of MHs. Higher-energy electrons are more likely to violate μ conservation in an MH, but only a few electrons are detected in this energy range. The measurement of these particles can be obscured by instrumental noise, making them difficult to resolve. This effect introduces uncertainty in the observations due to finite counting statistics (G. Nicolaou et al. 2024). Furthermore, the very short timescales associated with the quasilinear relaxation of the VDF through instabilities pose a challenge for the capturing of transient changes in the VDF with the current energy and time resolution of the available instruments. For instance, electron instabilities occur on timescales of order tens to hundreds of electron gyroperiods, corresponding to an approximate timescale of $10^{-2} \sim 10^{-1}$ s under our observed conditions (T. J. M. Boyd & J. J. Sanderson 2003). The Solar Orbiter SWA/EAS instrument records electron pitch-angle distributions at a cadence of 10 s. Consequently, we do not expect to observe a distinct bump feature in Figures 3 and 6. Due to this timescale separation, we cannot resolve the instability's growth phase directly. However, our observations provide sufficient indirect evidence for the occurrence of the proposed instability in the form of the detection of the unstable waves. In fact, the pitch-angle distribution shown in case 2 does not provide further insight into the electron behavior at the energy levels expected to trigger LWs. The spacecraft encounters a very small MH or merely crosses the boundary of a larger MH in this case. Panel (f) in Figure 5 provides a possible structure for this event, but the real structure may differ from our proposed representation.

Beyond the particle measurements, the wave detection is also constrained by instrumental limitations. The LW intensity may fall below the detection threshold of the spacecraft instrumentation, rendering the waves unobservable despite their presence, as suggested by case 2.

The specific trajectory with which the spacecraft crosses an MH is coincidental. Multispacecraft missions would be highly beneficial for studies like ours by enabling the determination of both the wavenumber of the observed waves and the three-dimensional morphology of the observed MHs. Resolving the wavevector of the unstable waves and the overall field geometry would help us confirm the resonance condition and provide deeper insights into the underlying physics (W. J. Sun et al. 2012; S. Huang et al. 2017; G. Wang et al. 2021).

4.3. Alternative Scenarios

MHs are complex structures in which multiple parameters of the ambient plasma change simultaneously. While we propose and test one possible mechanism that triggers LWs in MHs, different mechanisms may come into play depending on the nature of the MHs. For instance, density gradients can influence the electron behavior and trigger LWs, as shown in particle-in-cell simulations (R. Pechhacker & D. Tsiklauri 2014). In the majority of MHs, observations indicate an increase in number density as the magnetic field strength decreases to maintain pressure balance. However, these simulations explore density gradients that significantly exceed those observed in our cases. It would be worthwhile to adapt the simulations accordingly and to investigate the joint effects of field and density modulations on the electron VDF in realistic MHs.

Previous studies establish mechanisms for the generation of whistler waves in MHs (N. Ahmadi et al. 2018; W. Jiang et al. 2022; Z. Xu et al. 2025); however, we do not observe whistler waves in our presented cases. These previous analyses suggest that whistler waves are generated by time-evolving MHs, in which electron trapping, the generation of temperature anisotropy, or the formation of electron beams play key roles. In our cases, however, steady-state MHs create LWs through instability when strahl electrons encounter the MH structure. Therefore, we consider our cases complementary to the whistler-wave-emitting cases.

Other processes, such as betatron cooling (Z. Guo et al. 2021; W. Jiang et al. 2022) and magnetic pumping (E. Lichko & J. Egedal 2020), are reported in magnetospheric MHs. In our study, we do not observe such processes, which may be attributed to the distinct nature of quasi-stable MHs in the solar wind compared to those in the magnetosphere. It remains

unclear whether these observed differences arise from the intrinsic properties or size of the MHs under consideration or the properties of the strahl in the solar wind. They may also be partially due to limitations in the instrument resolution in our observations.

5. Conclusions

We propose a model to explain the excitation of LWs in solar wind MHs. Our model accounts for kinetic effects arising from the violation of the conservation of the magnetic moment that occurs when electrons from an asymmetric velocity distribution interact with localized magnetic field depressions.

Our model predicts conditions under which some of the suprathermal electrons break μ conservation in MHs when these MHs are sufficiently deep. By making reasonable assumptions about the size of the field structure, we derive the critical energy $E_{\rm crit}$ above which electrons break μ conservation for given pitch angles. Under certain conditions, these electrons create localized beams in the electron distribution that drive LWs through the bump-on-tail instability within the MHs.

We present observations from the Solar Orbiter spacecraft that are consistent with our model. They show LWs in regions for which our model predicts their occurrence. The observed frequencies of the enhancement in the electric field power spectrum agree with the predicted frequency from our model based on the analytical dispersion relation and the resonance velocity of the beam electrons created by violation of the μ conservation.

Although current spacecraft missions are limited in their capability to provide additional validation for our model, the cases shown here offer compelling evidence for our proposed explanation for LW-emitting MHs. While our study focuses on MHs in the solar wind, MHs in planetary magnetospheres and other plasma environments may show similar behavior. However, the requirement of the presence of an anisotropic suprathermal feature like the strahl makes solar wind MHs more likely to undergo our proposed mechanism. The violation of μ conservation in such environments could potentially trigger additional plasma processes beyond LW excitation due to the modification of the VDF.

Our work demonstrates that inhomogeneous field structures such as MHs play an important role in the transport of suprathermal electrons in collisionless plasmas. By establishing links between these structures and the particle behavior, our findings advance the understanding of energy conversion mechanisms. Furthermore, they highlight how magnetic structures critically define both particle distributions and wave activity in a plasma through the coupling of ion-scale and electron-scale kinetic processes. As extensions of our work, we propose statistical analyses based on our predictions and multipoint measurements with multispacecraft missions. This future work will advance our understanding of the excitation of LWs in solar wind MHs and similar multiscale couplings associated with plasma inhomogeneities.

Acknowledgments

This work was supported by STFC Consolidated Grant ST/W001004/1 and UKSA grant ST/X002012/1. This work was supported by the Royal Society (UK) and the Consiglio Nazionale delle Ricerche (Italy) through the International Exchanges Cost Share scheme/Joint Bilateral Agreement project "Multi-scale electrostatic energisation of plasmas: comparison of collective processes in laboratory and space" (award numbers IEC\R2\222050 and SAC.AD002.043.021). O.P. acknowledges the project "2022KL38BK-The ULtimate fate of TuRbulence from space to laboratory plAsmas (ULTRA)" (Master CUP B53D23004850006) by the Italian Ministry of University and Research, funded under the National Recovery and Resilience Plan (NRRP), Mission 4-Component C2-Investment 1.1, "Fondo per il Programma Nazionale di Ricerca e Progetti di Rilevante Interesse Nazionale (PRIN 2022)" (PE9) by the European Union—NextGenerationEU. W.J. is supported by the National Natural Science Foundation of China grant No. 42404177, the NSSC Youth Grant, and the Specialized Research Fund for State Key Laboratories of China.

ORCID iDs

Jingting Liu (刘婧婷) https://orcid.org/0009-0003-9856-5949
Daniel Verscharen https://orcid.org/0000-0002-0497-1096
Jesse Coburn https://orcid.org/0000-0002-2576-0992
Georgios Nicolaou https://orcid.org/0000-0003-3623-4928
Xiangyu Wu (吴翔宇) https://orcid.org/0000-0001-7019-5905
Wence Jiang (蒋文策) https://orcid.org/0000-0001-7431-5759
Oreste Pezzi https://orcid.org/0000-0002-7638-1706
Francesco Pucci https://orcid.org/0000-0002-5272-5404
Matteo Zuin https://orcid.org/0000-0002-0282-2978
Christopher J. Owen https://orcid.org/0000-0002-5982-4667
Hamish Reid https://orcid.org/0000-0002-6287-3494

References

Ahmadi, N., Wilder, F. D., Ergun, R., et al. 2018, JGRA, 123, 6383
Arrò, G., Califano, F., Pucci, F., Karlsson, T., & Li, H. 2024, ApJL, 970, L6
Arrò, G., Pucci, F., Califano, F., Innocenti, M. E., & Lapenta, G. 2023, ApJ, 958, 11
Baumjohann, W., & Treumann, R. A. 1996, Basic Space Plasma Physics (London: Imperial College Press)
Boldú, J., Graham, D., Morooka, M., et al. 2023, A&A, 674, A220
Boyd, T. J. M., & Sanderson, J. J. 2003, The Physics of Plasmas (Cambridge: Cambridge Univ. Press)
Burlaga, L., & Lemaire, J. 1978, JGRA, 83, 5157
Cairns, I. H. 1986, PASA, 6, 444
Chen, C., Liu, Y. D., & Hu, H. 2021, ApJ, 921, 15
Chen, F. F. 2016, Introduction to Plasma Physics (Cham: Springer)
Feldman, W., Asbridge, J., Bame, S., Montgomery, M., & Gary, S. 1975, JGR, 80, 4181
Ge, Y., McFadden, J., Raeder, J., et al. 2011, JGRA, 116, A01209
Guo, Z., Fu, H., Cao, J., et al. 2021, GeoRL, 48, e2021GL093826
Helgesen, G., Pieranski, P., & Skjeltorp, A. 1990, PhRvA, 42, 7271
Herr, W. 2016, arXiv:1601.05227
Horaites, K., Astfalk, P., Boldyrev, S., & Jenko, F. 2018, MNRAS, 480, 1499
Horbury, T., O'brien, H., Blazquez, I. C., et al. 2020, A&A, 642, A9
Huang, S., Du, J., Sahraoui, F., et al. 2017, JGRA, 122, 8577
Huang, S., Xu, S., He, L., et al. 2020, GeoRL, 47, e2020GL087515
Ichimaru, S. 1973, Basic Principles of Plasma Physics: A Statistical Approach (Boca Raton, FL: CRC Press)
Jiang, W., Verscharen, D., Jeong, S.-Y., et al. 2024, ApJ, 960, 30
Jiang, W., Verscharen, D., Li, H., Wang, C., & Klein, K. G. 2022, ApJ, 935, 169
Lapenta, G., & Bettarini, L. 2011, GeoRL, 38, L11102
Le Chat, G., Issautier, K., Meyer-Vernet, N., et al. 2009, PhPl, 16, 102903
Lichko, E., & Egedal, J. 2020, NatCo, 11, 2942
Lin, N., Kellogg, P., MacDowall, R., et al. 1995, GeoRL, 22, 3417
Lin, N., Kellogg, P. J., MacDowall, R., Tsurutani, B., & Ho, C. 1996, A&A, 316, 425
Lucek, E., Dunlop, M., Balogh, A., et al. 1999, GeoRL, 26, 2159

MacDowall, R., Lin, N., Kellogg, P., et al. 1996, in AIP Conf. Proc. 382, Proc. of the eigth int. solar wind conf.: Solar wind eight, ed. D. Winterhalter (Melville, NY: AIP Conf. Proc.), 301
Maksimovic, M., Bale, S., Chust, T., et al. 2020, A&A, 642, A12
Nicolaou, G., Livadiotis, G., & Ioannou, C. 2024, ApJ, 977, 168
Owen, C., Bruno, R., Livi, S., et al. 2020, A&A, 642, A16
Owen, C., Kataria, D., Berčič, L., et al. 2021, A&A, 656, L9
Pechhacker, R., & Tsiklauri, D. 2014, PhPl, 21, 012903
Pommois, K., Valentini, F., Pezzi, O., & Veltri, P. 2017, PhPl, 24, 012105
Pulupa, M., Bale, S. D., Badman, S. T., et al. 2020, ApJS, 246, 49
Robinson, P., & Benz, A. 2000, SoPh, 194, 345
Russell, C., Riedler, W., Schwingenschuh, K., & Yeroshenko, Y. 1987, GeoRL, 14, 644
Schroeder, J. M., Boldyrev, S., & Astfalk, P. 2021, MNRAS, 507, 1329
Shi, Q., Pu, Z., Soucek, J., et al. 2009, JGRA, 114, A10202
Soucek, J., Pìša, D., Kolmasova, I., et al. 2021, A&A, 656, A26
Sperveslage, K., Neubauer, F., Baumgärtel, K., & Ness, N. 2000, NPGeo, 7, 191
Sun, W. J., Shi, Q. Q., Fu, S. Y., et al. 2012, AnGeo, 30, 583
Tsurutani, B., Smith, E., Anderson, R., et al. 1982, JGRA, 87, 6060
Turner, J., Burlaga, L., Ness, N., & Lemaire, J. 1977, JGR, 82, 1921
Verscharen, D., Chandran, B. D., Boella, E., et al. 2022, FrASS, 9, 951628
Verscharen, D., Chandran, B. D., Jeong, S.-Y., et al. 2019a, ApJ, 886, 136
Verscharen, D., Klein, K. G., & Maruca, B. A. 2019b, LRSP, 16, 5
Wang, G., Volwerk, M., Wu, M., et al. 2021, AJ, 161, 110
Winterhalter, D., Neugebauer, M., Goldstein, B. E., et al. 1994, JGRA, 99, 23371
Xiao, T., Shi, Q., Tian, A., et al. 2014, SoPh, 289, 3175
Xu, Z., Wang, Z., Fu, H., et al. 2025, JGRA, 130, e2024JA033524
Yao, S., Shi, Q., Yao, Z., et al. 2019, GeoRL, 46, 523
Yu, L., Huang, S., Yuan, Z., et al. 2021, ApJ, 908, 56
Zhang, T., Russell, C., Baumjohann, W., et al. 2008, GeoRL, 35, L10106
Zhang, X.-J., Artemyev, A., Angelopoulos, V., & Horne, R. 2017, JGRA, 122, 10